



Natural sphalerite photocatalyst for treatment of oily wastewater produced by solvent extraction from spent lithium-ion battery recycling

Meirong Wu^a, Shaole Song^a, Tianyu Wang^a, Wei Sun^a, Shengming Xu^b, Yue Yang^{a,*}

^a School of Minerals Processing and Bioengineering, Central South University, Changsha 410083, China

^b Institute of Nuclear and New Energy Technology, Tsinghua University, Beijing 100084, China

ARTICLE INFO

Keywords:

Spent lithium-ion battery
Solvent extraction
Oily wastewater
Natural sphalerite
Photocatalyst

ABSTRACT

Oily wastewater from solvent extraction is hard to be treated due to a large number of organic pollutants and high salt content. Here, we found a photocatalyst (natural sphalerite (NS), (Zn, Fe)S) with great application potential for treating oily wastewater of solvent extraction, and studied its application in removal organics from actual solvent extraction wastewater of spent lithium-ion battery recycling. It found that doping Fe participated in the formation of new energy bands and accepted transferred-electrons from ZnS as electron acceptor, thus enhanced the visible-light absorption ability and carrier mobility. The photocatalysis activity of NS was further improved by adding hydrogen peroxide (H₂O₂), mainly because it prevented the recombination of photo-generated electron-hole pairs. Consequently, 86.20% removal of total organic carbon was achieved with H₂O₂-assisted NS under the optimum conditions. This work is expected to shed light on the application of photocatalysis in treatment of oily wastewater of solvent extraction.

1. Introduction

With the rise of portable electronic devices and new energy vehicles, the use of lithium-ion batteries (LIBs) has shown explosive growth [1,2]. The global production of LIBs reached \$22.4 billion in 2015 and \$45 billion in 2019 [3]. In China, the production of LIBs was \$15.3 billion in 2015 and increased to \$27.2 billion in 2019 [3]. The total global LIBs market demand is forecast to reach \$99.98 billion in 2025, and the shipment volume will reach 439.32 GWh [4]. The large-scale production and application of LIBs will inevitably lead to a large number of spent LIBs due to its limited-service life and the upgrade of electronic products [5]. If these spent LIBs are not properly disposed, the leakage of toxic organic electrolytes will cause serious environmental pollution on soil and groundwater. Meanwhile, spent LIBs contain high-value metals such as Li, Ni, Co, Mn, etc, among which Li and Co are rare metals and considered as important strategic resources [6]. According to the London Metal Exchange, the average price of Co in September 2021 was \$51712.27/t [7]. In addition, as an important raw material for synthesizing cathode materials for LIBs, the price of battery-grade Li₂CO₃ has nearly tripled in the past decade, reaching almost \$26,384/t in China in September 2021 [8]. The high metal content in spent LIBs is an important metal resource, especially in the case of limited global reserves,

about 86 million tons of Li and 25 million tons of Co [9]. Therefore, it is necessary and urgent to recycle spent LIBs for environmental protection and resource utilization.

Hydrometallurgical process is considered as one of the most suitable methods to recycle spent LIBs because of its high metal recovery rate, high product purity and low energy consumption [10]. Of hydrometallurgical techniques, solvent extraction has been widely applied for recovery of valuable metals from leachate of spent LIBs in practical industrial production [11]. However, a large amount of oily wastewater produces after solvent extraction because extractant can be entrained and miscible in the aqueous phase [12]. It is estimated that the extraction of one ton of metal from the leachate of spent LIBs will produce 20,000 liters of oily wastewater. Due to the toxicity and potential carcinogenicity of organics in these oily wastewaters, direct discharge them into environment poses a great threat to human health and ecosystem. Over the past decades, various approaches, such as activated carbon adsorption [13], froth flotation [14], membrane separation [15] and coagulation [16] have been studied to remove organics from oily wastewater. However, these methods have several disadvantages, such as high treatment costs, undesirable treatment efficiencies and recontamination problems. For example, activated carbon with good porosity and high specific surface area as an effective sorbent has been widely

* Corresponding author.

E-mail address: Eric1911@126.com (Y. Yang).

<https://doi.org/10.1016/j.apcatb.2022.121460>

Received 10 March 2022; Received in revised form 23 April 2022; Accepted 25 April 2022

Available online 28 April 2022

0926-3373/© 2022 Elsevier B.V. All rights reserved.

applied in the treatment of oily wastewater [13], but a complex regeneration process is needed to maintain the original adsorption performance [17]. Froth flotation is the use of tiny bubbles to attach suspended oil particles in water to realize oil-water separation, which is easy to apply, but cannot effectively remove emulsified oil [14]. Membrane filtration is capable of removing small oil droplets and larger than 0.005 μm hydrocarbons, but membrane fouling limits the application of this technology [18]. Coagulation can remove emulsified oil, dissolved oil and some organic polymers by adsorption, bridge and crosslinking, but it is difficult to screen high-efficiency coagulants for specific treatment [19]. Hence, it is crucial for spent LIBs recycling to develop more efficient and green technologies to treat oily wastewater.

Photocatalysis can generate reduction electrons (e^-) and oxidation holes (h^+) by absorbing visible/UV light from solar radiation, which has been considered as an advanced and pollution-free oxidation method for treating oily wastewater from various industries [20–22]. Consequently, various semiconductors were proposed as photocatalysts for photocatalytic degradation of pollutants. Kang et al. [23] investigated the performance of a vacuum ultraviolet and TiO_2 oxidation system for the photocatalytic pretreatment of oily wastewater from the restaurant. Maximum COD removal (63%) was achieved under the optimum conditions of irradiation 10 min and the final COD decreased from 3981 to 1473 mg/L. Zhou et al. [24] proposed hydrothermal synthesis of W/Mo co-doped BiVO_4 particles to degrade partially hydrolyzed polyacrylamide in oily wastewater from polymer flooding process and got 65% COD removal after 180 min of UV–vis light irradiation. Hu et al. [25] synthesized ZnO nanocrystal by a sonochemical method and their photocatalytic degradation of diesel pollutants in seawater was 84% in 180 min when the concentration of hydrogen peroxide (H_2O_2) was 0.16%. However, photocatalytic degradation of organics in the oily wastewater with high salt content usually shows extremely low activity, which is due to the instability of these nano-photocatalysts affected by anions and easy to aggregate into large particles [26]. Ascribed to the million-years geological process, natural sphalerite (NS) possesses stable physical and chemical properties in comparison of the traditional chemical process [27,28]. It can be obtained with low cost. Moreover, NS contains various impurity elements and complicated crystal lattice defects, which could cause even longer wavelength being absorbed to induce more e^- – h^+ pairs, suggesting a great potential in practical application [29,30]. As a result, NS might be a photocatalyst of choice to tackle these difficulties, although reports on the application of NS photocatalysis in the oily wastewater of solvent extraction are lacking.

In this work, we report the use of NS photocatalysis to removal organics from actual solvent extraction wastewater of spent LIBs. On this catalyst, the d-orbitals from Fe were involved in the formation of the new valence and conduction band, thus changed the semiconductor type of ZnS from p-type to n-type. Moreover, the electron transfer between Fe and S was more obvious than that between Zn and S, which could facilitate the transfer of the photo-generated e^- from ZnS to Fe and achieved a spatial separation of e^- – h^+ pair. Promoted by these features, $(\text{Zn}_{0.72}\text{Fe}_{0.28})\text{S}$ exhibited superior visible-light absorption ability and carrier mobility. Consequently, 86.20% TOC removal was achieved with H_2O_2 -assisted $(\text{Zn}_{0.72}\text{Fe}_{0.28})\text{S}$ under the optimum conditions.

2. Experimental section

2.1. Materials and reagent

The natural sphalerite samples with different Fe content used in this study were collected from different deposits in China. After mechanically crushed and milled by with crusher (JC6, Beijing Grinder Instrument Equipment Co., Ltd, China) and mill (WZM-1 L, Jinyun Mining Machinery Factory, China), the resultant particles were then passed through 400-mesh sieves to obtain sphalerite powder with particle sizes < 38 μm . The mineral sample preparation process is shown in Fig. S1. The raw wastewater used in this study was collected from a spent LIBs

recycling plant in China. A brief flow diagram of recycling spent LIBs and the source of raw wastewater is shown in Fig. S2. Recycling process for LIBs generally needs two typical processes: pretreatments and hydrometallurgical processes. Pretreatments processes include discharging, dismantling, separation, etc. Leaching, chemical precipitation and solvent extraction are usually involved in the hydrometallurgical processes. The oily wastewater is the residual solution after the extraction of Ni, Co and Mn in the spent LIBs leaching solution, which mainly contains 2-ethylhexyl phosphoric acid mono(2-ethylhexyl) ester (P507) extractant, di(2-ethylhexyl) phosphoric acid (P204) extractant and 260# solvent oil. The main physicochemical characteristics of the raw wastewater are shown in Table S1. Hydrochloric acid (HCl, 36.0 ~ 38.0 wt%) and H_2O_2 (30 wt%) used in this experiment were purchased from Sinopharm Chemical Reagent Co. Ltd. All the reagents are analytical grade and used without further treatment.

2.2. Photocatalytic reactions

Photodegradation experiments were carried out in a 150 mL double-layer beaker reactor at room temperature. First, the catalyst was dispersed in 100 mL of oily wastewater from hydrometallurgical recycle of spent LIBs. The pH of the suspension was adjusted by adding HCl. Before irradiation, the suspension was magnetically stirred for 30 min in the dark to establish the adsorption–desorption equilibrium. Then, required amount of H_2O_2 was added into the solution to initiate the photocatalytic reaction. A 300 W Xenon lamp (PLS-SXE300, Beijing Perfect Light, China) with 420 nm cut-off filter was used as the visible light source, which was placed 8 cm away from the liquid level. The light intensity was measured by a UV-A radiometer (PL-MW2000, Beijing Perfect Light, China). The outer wall of the photocatalytic reactor was cooled with circulating water by a thermostat water bath to keep the reaction temperature at room temperature. The experimental apparatus used for carrying out the photocatalytic reactions is shown in Fig. S4. After visible light irradiation for certain time, 5.0 mL suspension was filtrated with a 0.45 μm membrane immediately, diluted 10 times for determining the concentration by TOC. The removal efficiency of TOC is calculated according to the following formula:

$$R(\%) = \frac{C_0 - C_t}{C_0} \times 100 \quad (1)$$

where $R(\%)$ is the removal efficiency, C_0 (mg/L) is the initial concentration of TOC, and C_t (mg/L) is the concentration of TOC at time t .

2.3. Measurement and characterization

The chemical composition of the sphalerite samples was determined using an X-ray fluorescence spectrum method (XRF, PANalytical Axios, Netherlands). The crystal structures of the samples were characterized using an X-ray diffraction spectrometer (XRD, X'Pert PRO MPD, Netherlands) equipped with $\text{Cu K}\alpha$ irradiation ($\lambda = 1.5406 \text{ \AA}$). The morphologies were observed by scanning electron microscopy (SEM, Zeiss Supra 55, Germany) with energy dispersive X-ray spectrometer (EDS). X-ray photoelectron spectroscopy (XPS) were obtained with Thermo ESCALAB 250XI Scanning X-ray Microprobe TM and VB-XPS was measured at the same condition. The specific surface area and pore size distribution were tested by Nitrogen adsorption–desorption measurements at 77 K (AUTOSORB IQ, USA). UV–Vis spectrophotometer (Lambda 750 PE) with an integrating sphere from 200 to 800 nm was used to record UV–Vis diffuse reflection spectrum (UV–Vis DRS) of NS. The photoluminescence (PL) spectra of the samples were obtained at room temperature by a spectrofluorometer (FLS1000, England) with an excitation wavelength of 350 nm. The Mott-Schottky (MS) plots, transient photocurrent responses and electrochemical impedance spectroscopy (EIS) were measured by a CHI-660E (Chenhua, Shanghai) electrochemical workstation with a standard three-electrode system.

The working electrode was the materials depositing on an ITO conducting glass. The Ag/AgCl electrode and Pt wire were used as reference electrode and counter electrode, respectively. The measured potentials versus Ag/AgCl were converted to the normal hydrogen electrode (NHE) scale by $E_{\text{NHE}} = E_{\text{Ag/AgCl}} + 0.197$. Electron paramagnetic resonance (EPR, Bruker EMXPLUS) was used to detect photo-generated hole (h^+), superoxide radical ($\cdot\text{O}_2^-$), and hydroxyl radical ($\cdot\text{OH}$) under visible-light irradiation ($\lambda > 420$ nm). The trapping agent 2,2,6,6-tetramethylpiperidine-1-oxyl (TEMPO) was used to detect h^+ in water solution. TEMPO essentially shows EPR signal due to the unpaired electrons of carbon atoms in aromatic nuclei, and if the catalyst produces h^+ (h^+ can be combined with single electrons in TEMPO), the signal will be weakened. The trapping agent 5,5-dimethyl-1-pyrroline N-oxide (DMPO) was used to capture $\cdot\text{OH}$ in water solution and to capture $\cdot\text{O}_2^-$ in methanol solution, respectively. The mineralization rate of organics was determined using a Total Organic Carbon (TOC) analyzer (TOC-L, Shimadzu, Japan). The organic compounds in the wastewater were measured by Three-dimensional excitation–emission matrix (3D-EEM) fluorescence spectroscopy (F7000, Hitachi, Tokyo, Japan) at the excitation emission wavelengths (Ex/Em) = (200–550 nm/250–600 nm) and ultrapure water was used as the blank.

2.4. Theoretical calculation

The effects of Fe atoms on the band structure and semiconducting properties of sphalerite were investigated with density functional theory (DFT) calculations. We employed the Vienna Ab Initio Package (VASP) to perform all the density functional theory (DFT) calculations within the generalized gradient approximation (GGA) using the PBE formulation. We chose the projected augmented wave (PAW) potentials to describe the ionic cores and take valence electrons into account using a plane wave basis set with a kinetic energy cutoff of 400 eV. Partial occupancies of the Kohn–Sham orbitals were allowed using the Gaussian smearing method and a width of 0.05 eV. The electronic energy was considered self-consistent when the energy change was smaller than 10^{−5} eV. A geometry optimization was considered convergent when

the force change was smaller than 0.02 eV/Å. The equilibrium lattice constant of cubic zincblende-type ZnS unit cell was optimized, when using a $9 \times 9 \times 9$ Monkhorst-Pack k-point grid for Brillouin zone sampling to be $a = 5.448$ Å. We then use it to construct a $2 \times 2 \times 3$ supercell model (model 1). This supercell comprises of 48 Zn and 48 S atoms. We also construct a Fe-doped model (model 2) by replacing 13 Zn atoms by Fe atoms. Fe atoms were distributed as evenly as possible. During structural optimizations, the gamma point in the Brillouin zone was used for k-point sampling, and all atoms allowed to relax. For model 2, the volume of the supercell was also optimized and it equilibrates at $10.64 \times 10.64 \times 15.96$ Å³. The charge density differences were created by VESTA visualization code and calculated as $\Delta\rho(r) = \rho_{\text{total}}(r) - \rho_{\text{Fe-SA}}(r) - \rho_{\text{ZnS}}(r)$, where $\rho_{\text{total}}(r)$ is the electron density of Fe-doped ZnS, $\rho_{\text{Fe-SA}}(r)$ is the electron density of isolated Fe single atom, and $\rho_{\text{ZnS}}(r)$ is the electron density of ZnS. The model of the supercell is shown in Fig. S3.

3. Results and discussion

3.1. Structure of prepared materials

The crystal chemical formula of the NS samples could be approximately expressed as $(\text{Zn}_{0.98}\text{Fe}_{0.02})\text{S}$, $(\text{Zn}_{0.96}\text{Fe}_{0.04})\text{S}$ and $(\text{Zn}_{0.72}\text{Fe}_{0.28})\text{S}$, respectively (Table S1). As indicated in Fig. 1a, the main diffraction peaks of $(\text{Zn}_{0.98}\text{Fe}_{0.02})\text{S}$ at $2\theta = 28.54^\circ$, 33.08° , 47.47° , 56.31° , 69.41° and 76.68° can be indexed to (111), (200), (220), (311), (400) and (331) planes for cubic phase of ZnS planes (JCPDS card, No. 05–0566), respectively. It is noteworthy that the XRD diffraction peaks continuously shift to the low angle region with the increase of Fe content in sphalerite. For example, the (111) plane of $(\text{Zn}_{0.96}\text{Fe}_{0.04})\text{S}$ and $(\text{Zn}_{0.72}\text{Fe}_{0.28})\text{S}$ moved to 28.537° and 28.487° , respectively, compared with $2\theta = 28.538^\circ$ for $(\text{Zn}_{0.98}\text{Fe}_{0.02})\text{S}$ (Fig. 1b). It implied that Fe was incorporated into the lattice of sphalerite and increased the fringe lattice distance of sphalerite crystal due to the larger ion radius of Fe^{2+} (0.76 Å) than that of Zn^{2+} (0.74 Å) [31]. The lattice parameter of $(\text{Zn}_{1-x}\text{Fe}_x)\text{S}$ ($x = 0.02, 0.04, 0.28$) samples were 5.4122, 5.4147 and 5.4232 Å,

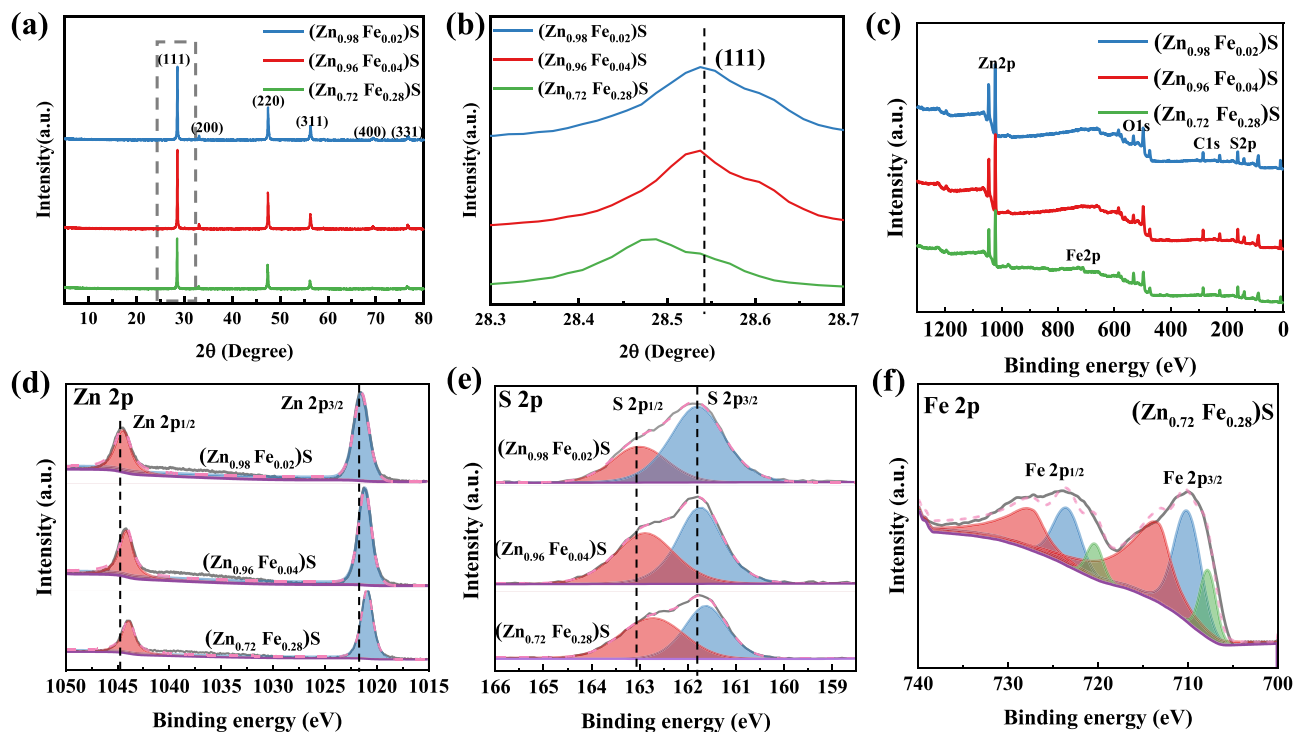


Fig. 1. (a) XRD patterns; (b) XRD patterns at the (111) plane of $(\text{Zn}_{1-x}\text{Fe}_x)\text{S}$ samples. (c) XPS survey spectra; high-resolution XPS spectra of (d) Zn 2p, (e) S 2p of $(\text{Zn}_{1-x}\text{Fe}_x)\text{S}$ samples and (f) Fe 2p of $(\text{Zn}_{0.72}\text{Fe}_{0.28})\text{S}$.

respectively, which were larger than that of ZnS (JCPDS 05–0566; $a_0 = 5.4060 \text{ \AA}$), consistent with the above mentioned the increase of fringe lattice distance of sphalerite. The lattice parameter of sphalerite increases with Fe content because the increased content of FeS will increase the ionic bonding in sphalerite [32]. The calculated crystallite sizes of $(\text{Zn}_{0.98}\text{Fe}_{0.02})\text{S}$, $(\text{Zn}_{0.96}\text{Fe}_{0.04})\text{S}$ and $(\text{Zn}_{0.72}\text{Fe}_{0.28})\text{S}$ according to Scherrer equation (Eq. S1) were 50.66, 51.81, 57.36 nm, respectively. The larger crystallite sizes of $(\text{Zn}_{0.98}\text{Fe}_{0.02})\text{S}$ and $(\text{Zn}_{0.96}\text{Fe}_{0.04})\text{S}$ than that of $(\text{Zn}_{0.72}\text{Fe}_{0.28})\text{S}$ was further proved that the lattice expansion with the increase of Fe content in sphalerite. Lattice expansion may cause lattice deformation, thus changes the electronic structure of sphalerite and in turn affect the semiconducting property and photocatalytic activity of sphalerite.

The XPS survey spectra in Fig. 1c showed the existence of Zn and S elements in $(\text{Zn}_{1-x}\text{Fe}_x)\text{S}$ series samples. Because of the low Fe content in $(\text{Zn}_{0.98}\text{Fe}_{0.02})\text{S}$ and $(\text{Zn}_{0.96}\text{Fe}_{0.04})\text{S}$, it cannot be detected by XPS, and element Fe only appeared in the XPS spectra of $(\text{Zn}_{0.72}\text{Fe}_{0.28})\text{S}$. The high-resolution XPS spectra of Zn 2p, S 2p, Fe 2p are shown in Fig. 1d-f. In Zn 2p of $(\text{Zn}_{0.98}\text{Fe}_{0.02})\text{S}$, there were two symmetric peaks centered at 1021.56 eV and 1044.57 eV corresponds to Zn 2p_{3/2} and Zn 2p_{1/2}, respectively [33]. The S 2p of $(\text{Zn}_{0.98}\text{Fe}_{0.02})\text{S}$ can be fitted into two peaks located at 161.80 eV and 162.98 eV, which were attributed to S 2p_{3/2} and S 2p_{1/2} [34,35], respectively. It was worth noting that comparing the peaks of $(\text{Zn}_{0.98}\text{Fe}_{0.02})\text{S}$ in XPS spectra of Zn 2p and S 2p, the peaks of $(\text{Zn}_{0.96}\text{Fe}_{0.04})\text{S}$ and $(\text{Zn}_{0.72}\text{Fe}_{0.28})\text{S}$ were shifted toward lower binding energies, which may be due to the influence of the bond between Fe and S on the electronic environments of the Zn cation and S anion [36]. For high-resolution XPS spectra of Fe 2p (Fig. 1f), two main peaks assigned to Fe 2p_{3/2} and Fe 2p_{1/2} were observed at 711.0 eV and 724.7 eV, respectively [37]. For Fe 2p_{3/2}, the peaks at 712.8 eV, 710.04 eV and 707.76 eV correspond to Fe²⁺ bonded with S²⁻ [38,39], confirming the presence of FeS in the sphalerite. These XPS results indicated that the Fe doping in sphalerite result in a shift in the binding energy of the material, which may change the direction of electron transfer between Zn, Fe, and S and accelerate the separation of e⁻-h⁺ pairs.

The morphology and distribution of elements of $(\text{Zn}_{1-x}\text{Fe}_x)\text{S}$ samples are shown in Fig. 2. These samples exhibited irregular shaped particles and significant heterogeneity of particle size in the presence of Zn, S and Fe elements. The surface area of the samples slightly decreased with the increase of Fe content, while the pore volumes as well as the pore sizes do not change significantly (Fig. S5 and Table S2). Besides, the

cleavage planes and fracture surfaces can be clearly seen. The surface reactivity of natural mineral is usually higher than that of their synthetic counterparts with perfect crystal planes, because cleavage and fracture planes provide more active sites than plane crystal planes [30].

3.2. Optical property

The UV-Vis DRS of $(\text{Zn}_{1-x}\text{Fe}_x)\text{S}$ samples is displayed in Fig. 3a. Notably, $(\text{Zn}_{0.98}\text{Fe}_{0.02})\text{S}$, $(\text{Zn}_{0.96}\text{Fe}_{0.04})\text{S}$ and $(\text{Zn}_{0.72}\text{Fe}_{0.28})\text{S}$ all responded over the entire visible wavelength range (380–780 nm). It was also obvious that $(\text{Zn}_{1-x}\text{Fe}_x)\text{S}$ exhibited a red shift and absorption increases in the visible light range with the increase of Fe content. According to Eq. S2, the bandgap energy (E_g) of $(\text{Zn}_{0.74}\text{Fe}_{0.26})\text{S}$, $(\text{Zn}_{0.48}\text{Fe}_{0.52})\text{S}$ and $(\text{Zn}_{0.24}\text{Fe}_{0.76})\text{S}$ photocatalyst were calculated as 3.15, 3.03 and 2.03 eV (Fig. 3b), respectively, confirming that the sample with higher Fe has a wider visible light response due to its narrower E_g . It is well known that pure sphalerite is wide band gap semiconductors ($\sim 3.6 \text{ eV}$), but FeS has a very narrow E_g ($\sim 0.1 \text{ eV}$) [40]. Thus, increasing the content of Fe in sphalerite will promote the absorption of visible light and narrow E_g . Fig. 3c showed the valence band (VB) XPS of the $(\text{Zn}_{1-x}\text{Fe}_x)\text{S}$ samples, and the valence band energies (E_{VB}) of $(\text{Zn}_{0.98}\text{Fe}_{0.02})\text{S}$, $(\text{Zn}_{0.96}\text{Fe}_{0.04})\text{S}$ and $(\text{Zn}_{0.72}\text{Fe}_{0.28})\text{S}$ were 0.96, 0.92 and 0.73 eV, respectively. According to Eq. S3, the conduction band energies (E_{CB}) potential values of these samples were -2.19 , -2.11 and -1.30 eV , respectively. The MS plots of $(\text{Zn}_{1-x}\text{Fe}_x)\text{S}$ further proved the above calculation about the energy band was valid (Fig. S6). The E_{VB} of $(\text{Zn}_{1-x}\text{Fe}_x)\text{S}$ samples were more negative than the redox potential of $\cdot\text{OH}/\text{H}_2\text{O}$ ($+2.27 \text{ eV}$ vs NHE) [41]. Therefore, the photo-generated h⁺ left in VB of $(\text{Zn}_{1-x}\text{Fe}_x)\text{S}$ could directly oxidize and degrade organic pollutants instead of reacting with H₂O to form $\cdot\text{OH}$. Similarly, the E_{CB} potential values of these samples were more negative than the redox potential of $\cdot\text{O}_2/\text{O}_2$ (-0.33 eV vs NHE) [41]. Hence, the photo-generated e⁻ left in CB of $(\text{Zn}_{1-x}\text{Fe}_x)\text{S}$ can react with the adsorbed O₂ to form $\cdot\text{O}_2$. In order to further explore the electronic structure variations of ZnS after the doping of Fe, the band structure and density of states (DOS) were investigated by DFT calculations (Fig. 3d-g). The calculated E_g value (0.90 eV) of $(\text{Zn}_{0.72}\text{Fe}_{0.28})\text{S}$ was less than the experimental value of 2.03 eV, which was ascribed to the drawbacks of the generalized gradient approximation (GGA) method that often underestimates the E_g [42]. The band structures and DOS showed that some new orbitals energy levels appear on the CB and VB and result in the descent of CB position and the ascent of the VB position. The CB was

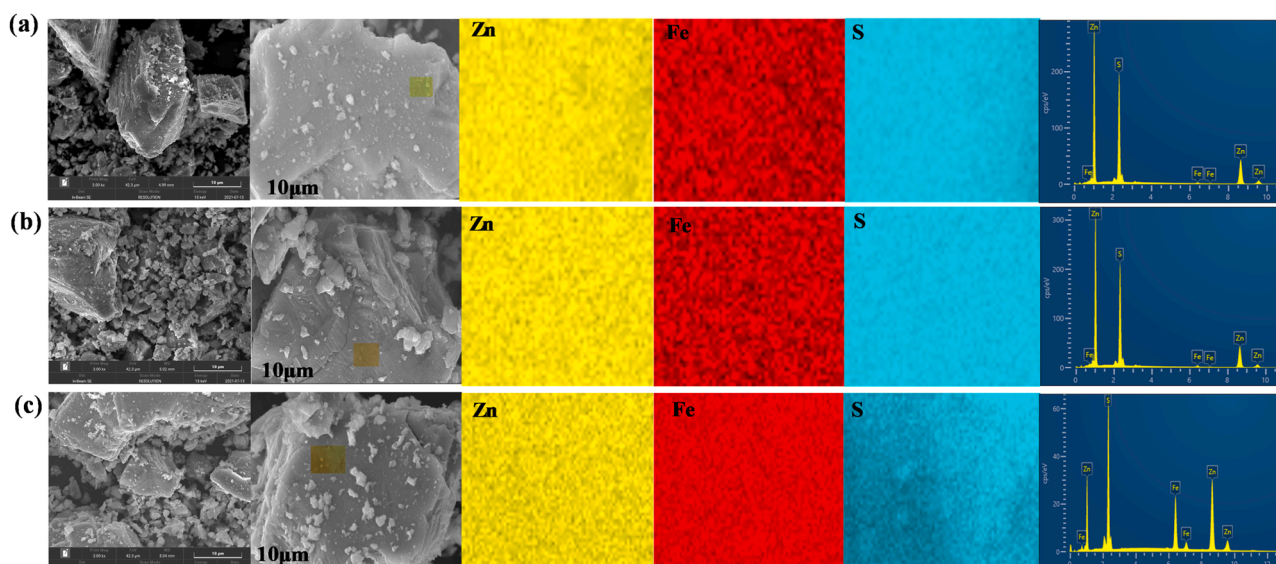


Fig. 2. Scanning electron microscopy (SEM) images and X-ray spectrometer (EDS) mapping images of (a) $(\text{Zn}_{0.98}\text{Fe}_{0.02})\text{S}$, (b) $(\text{Zn}_{0.96}\text{Fe}_{0.04})\text{S}$ and (c) $(\text{Zn}_{0.72}\text{Fe}_{0.28})\text{S}$.

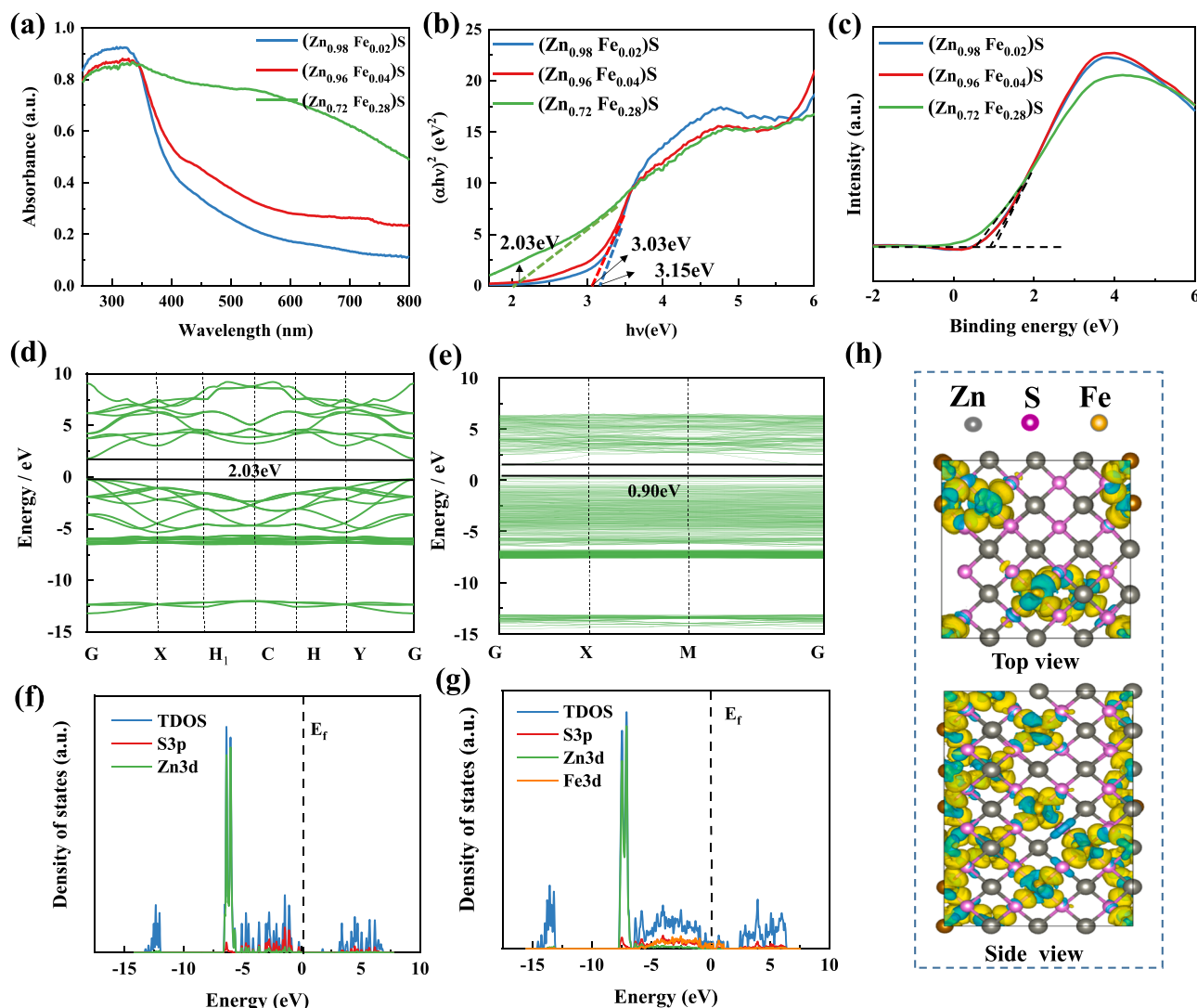


Fig. 3. (a) UV-vis DRS spectra of (Zn_{1-x}Fe_x)S samples; (b) The calculated E_g values of (Zn_{1-x}Fe_x)S samples; (c) Valence-Band XPS spectra; Band structure of (d) perfect ZnS and (e) (Zn_{0.72}Fe_{0.28})S; DOS (total density of states (TDOS) and partial density of Zn 3d, Fe 3d and S 3p states (PDOS)) of (f) perfect ZnS and (g) (Zn_{0.72}Fe_{0.28})S, the dashed lines represent the Fermi level at 0 eV; (h) Electron density difference diagram of (Zn_{0.72}Fe_{0.28})S.

mainly composed of p-orbitals of the S atoms, while the d-orbitals of Zn contribute to the VB of ZnS. After the doping of Fe, the d-orbitals of Fe atoms participate in the composition of VB, which weaken oxidative capacity of holes to a large extent by raising the VB position, thus protect sphalerite from photocorrosion [43]. In addition, the original blank energy region located at ZnS bandgap was partially occupied with Fe 3d orbitals, which resulted in excited electrons after illuminating in ZnS transferring to Fe. Moreover, the doping Fe made the Fermi level shift to a higher energy level and changed the semiconductor type of sphalerite from p-type to n-type, which increased the electron density in favor of the optical adsorption and carrier transfer of ZnS [44,45]. As a consequence, more active species would be produced to degrade organic pollutants in photocatalysis. In order to determine the direction of electron transfer, DFT were also used to study the electron density difference of (Zn_{0.72}Fe_{0.28})S, and the result is shown in Fig. 3h. The electronegativity of atoms in the crystal (Zn: 1.65, Fe: 1.83, S: 2.58) is different from that of external electrons, so the electrons may rearrange after Fe doping or substitution [44]. Fig. 3h showed S atoms bonded with Fe obviously accumulated electrons, causing an uneven charge distribution in the lattice structure. This mean that ZnS acted as an electron donor to transfer electrons to the electron acceptor Fe, which could facilitate the spatial separation of photo-generated e^- - h^+ pair.

To fully understand the transfer ability of photo-generated charge, the EIS analysis was carried out and the result is shown in Fig. 4a. As seen in Fig. 4a, (Zn_{0.72}Fe_{0.28})S with the minimum impedance has the highest charge transfer ability among all the samples. This indicated that the substitution of Fe enhanced the interfacial charge transfer of catalysts, and was conducive to the reaction between e^- and H₂O₂. The transient photocurrent response was usually used to evaluate the total amount of e^- and h^+ generation by catalyst [46]. Fig. 4b showed the relationship between photocurrent and time curves of (Zn_{0.98}Fe_{0.02})S, (Zn_{0.96}Fe_{0.04})S and (Zn_{0.72}Fe_{0.28})S with four on and off intermittent excitation cycles. The photocurrent response of the (Zn_{0.72}Fe_{0.28})S was considerably higher than those of (Zn_{0.98}Fe_{0.02})S and (Zn_{0.96}Fe_{0.04})S. In particular, the photocurrent of (Zn_{0.72}Fe_{0.28})S can be maintained at 0.13 mA/cm² after four cycles, five times higher than that of (Zn_{0.98}Fe_{0.02})S, which demonstrated more efficient charge transportation and separation. The transient photocurrent response analysis well agrees with E_g and EIS measurement.

PL spectroscopy was conducted to further evaluate the separation efficiency of catalyst e^- - h^+ pairs. In general, a lower PL intensity indicates that the recombination of photo-generated e^- and h^+ is relatively low, resulting in a higher photocatalytic activity [47]. It can be seen from Fig. 4c that (Zn_{0.98}Fe_{0.02})S and (Zn_{0.96}Fe_{0.04})S have a strong

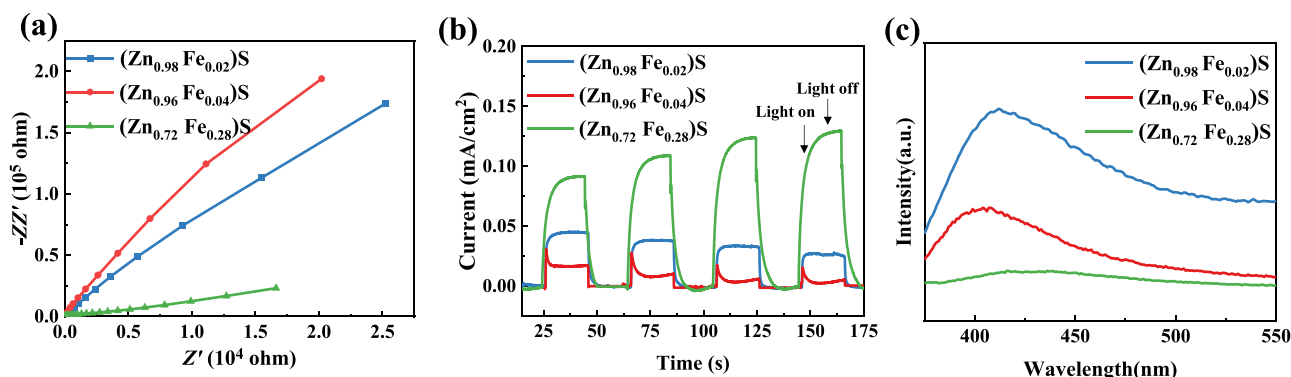


Fig. 4. (a) EIS; (b) transient photocurrent response; (c) PL spectra of the $(\text{Zn}_{1-x}\text{Fe}_x)\text{S}$ samples under an excitation wavelength of 350 nm.

emission peak at about 410 nm, which can be attributed to the quick recombination of e^- and h^+ . $(\text{Zn}_{0.72}\text{Fe}_{0.28})\text{S}$ showed a weaker PL intensity than $(\text{Zn}_{0.98}\text{Fe}_{0.02})\text{S}$ and $(\text{Zn}_{0.96}\text{Fe}_{0.04})\text{S}$, indicating that as the increase of Fe content in sphalerite, the recombination of e^- – h^+ pairs was prevented, resulting in an enhancement in the photocatalytic activity.

3.3. Photocatalytic performance under visible light irradiation

In Fig. 5a, there was no obvious TOC removal in the absence of photocatalysts (blank control group), indicating that the organic pollutants in the oily wastewater were stable under visible light. The removal efficiency of TOC by adsorption–desorption in $(\text{Zn}_{0.98}\text{Fe}_{0.02})\text{S}$, $(\text{Zn}_{0.96}\text{Fe}_{0.04})\text{S}$ and $(\text{Zn}_{0.72}\text{Fe}_{0.28})\text{S}$ in the dark were 4.15%, 4.06%, and 3.72%, respectively. Obviously, $(\text{Zn}_{0.72}\text{Fe}_{0.28})\text{S}$ displayed superior photocatalytic activity compared with the above samples and 51.27% of TOC was removed within 180 min. The excellent photocatalytic activity of $(\text{Zn}_{0.72}\text{Fe}_{0.28})\text{S}$ is due to its superior light absorption capability, charge transfer performance and charge separation ability. However, photocatalysis of natural minerals alone is not enough to effectively remove organics from oily wastewater– H_2O_2 was added to capture the photo-induced e^- and prevent the recombination of e^- – h^+ pairs, thus improving the degradation efficiency of organic pollutants. As shown in Fig. 5b, the sole application of H_2O_2 under dark condition and visible light irradiation after 180 min provided only 17.17% and 21.28% TOC removal, respectively, which was mainly attributed to the oxidation of H_2O_2 itself. When $(\text{Zn}_{1-x}\text{Fe}_x)\text{S}$ samples were added without visible light irradiation in the presence of H_2O_2 , the removal efficiencies of TOC by $(\text{Zn}_{0.98}\text{Fe}_{0.02})\text{S}$, $(\text{Zn}_{0.96}\text{Fe}_{0.04})\text{S}$ and $(\text{Zn}_{0.72}\text{Fe}_{0.28})\text{S}$ were approximately 40.27%, 48.64% and 59.15%, respectively, indicating that H_2O_2 can be activated by sphalerite. More importantly, the TOC removal efficiency

with $(\text{Zn}_{1-x}\text{Fe}_x)\text{S}$ samples were further increased to 50.16%, 60.79% and 86.20% under visible light in the presence of H_2O_2 , respectively.

The effects of $(\text{Zn}_{0.72}\text{Fe}_{0.28})\text{S}$ dosage, H_2O_2 concentration, visible light (VL) intensity and solution pH on the TOC removal efficiency were investigated in the $(\text{Zn}_{0.72}\text{Fe}_{0.28})\text{S}/\text{H}_2\text{O}_2/\text{vis}$ system (Fig. S7). In conclusion, the optimal conditions for TOC removal are 2 g/L NS, 0.2 mol/L H_2O_2 , 101.5 $\text{mW}\cdot\text{cm}^{-2}$ VL intensity and $\text{pH} = 3.0$. At the optimal conditions, the TOC removal efficiency was 86.20% and the concentrations of leached Fe and Zn left in solution were only 1.47 mg/L and 9.85 mg/L, respectively. The reusability of $(\text{Zn}_{0.72}\text{Fe}_{0.28})\text{S}$ in the $(\text{Zn}_{0.72}\text{Fe}_{0.28})\text{S}/\text{H}_2\text{O}_2/\text{vis}$ system was evaluated by five cycles experiments (Fig. S8a). The TOC removal decreased after each recycle and its removal efficiency decreased to 43.74% after five cycles. This may be related to the catalyst inactivation after the reaction. Besides, no apparent changes of the XRD pattern of $(\text{Zn}_{0.72}\text{Fe}_{0.28})\text{S}$ before and after using were observed (Fig. S8b), implying no obvious photocorrosion occurred during the irradiation process for $(\text{Zn}_{0.72}\text{Fe}_{0.28})\text{S}$.

3.4. Identifying changes in characteristics and content of organic compounds

The organic compounds in the oily wastewater before and after treatment were characterized by 3D-EEM spectrum scanning (Fig. 6). According to the type and location of the fluorescent compounds, the fluorescence spectrum was divided into five regions (Text S1). As shown in Fig. 6a, the 3D-EEM spectrum of the oily wastewater was mainly located in the humic acid-like V area, which means humic acid-like was the main component. Obviously, there were two main luminescence regions in the soluble microbial products IV area and humic acid-like V area, namely F_1 (Ex/Em = 240–300 nm/350–400 nm) and F_2 (Ex/Em = 300–360 nm/390–450 nm). F_1 was the fluorescent peak of fulvic acid in

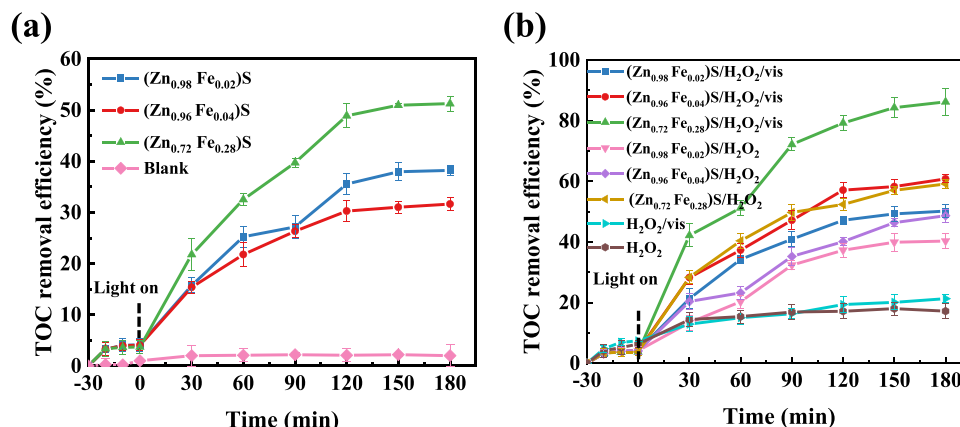


Fig. 5. (a) TOC removal efficiency changes with time in different catalysts under visible light irradiation; (b) TOC removal efficiency in the different reaction system.

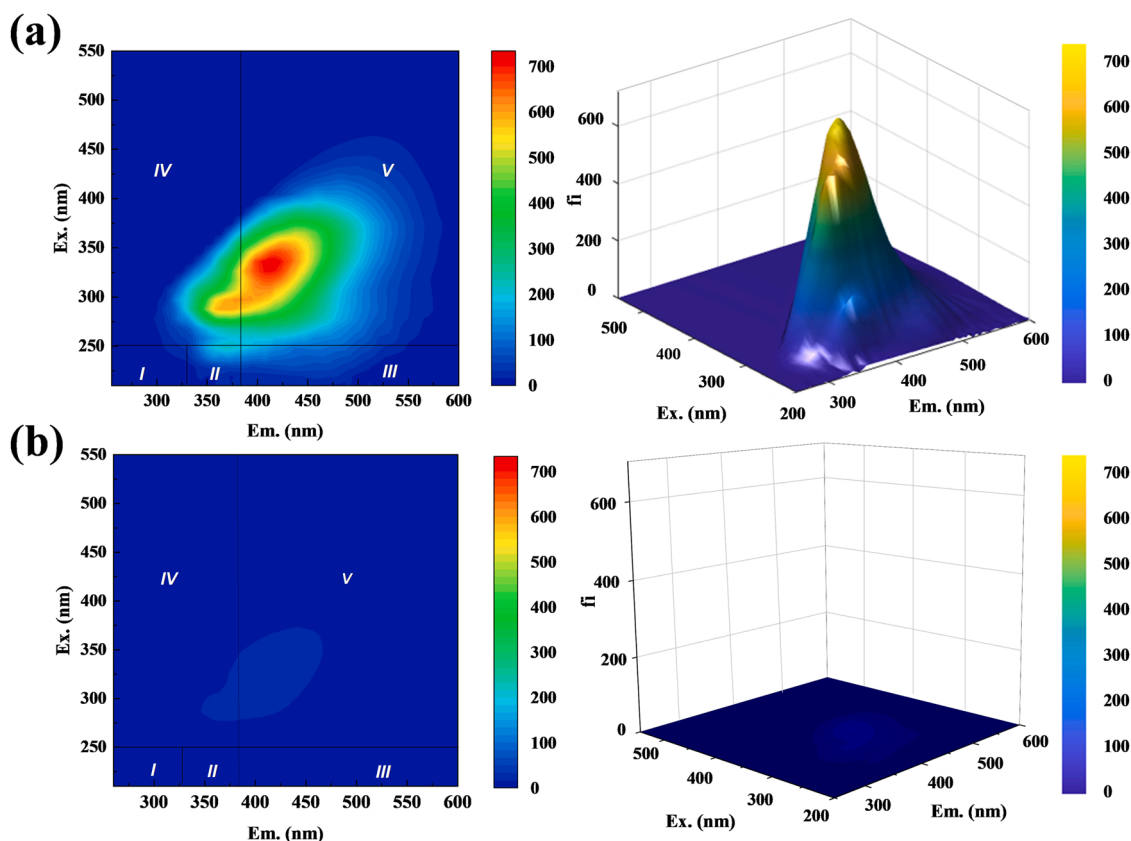


Fig. 6. 3D-EEM spectrum of the oily wastewater (a) before treatment and (b) after treatment.

the ultraviolet region, which was mainly produced by organic phosphate substances with low molecular weight and high fluorescence efficiency [48]. F_2 was the fluorescence peak of humic acid in the visible region, which was mainly caused by polycyclic aromatic substances with high molecular weight and high stability [48]. The fluorescence intensity of the wastewater in the visible region was high, indicating that the oily wastewater of solvent extract from spent LIBs recycling can represent the typical refractory wastewater [49].

As seen from Fig. 6b that after 180 min treatment with $(\text{Zn}_{0.72}\text{Fe}_{0.28})\text{S}/\text{H}_2\text{O}_2/\text{vis}$ system, the fluorescence peak F_1 of fulvic acid in the ultraviolet region and the fluorescence peak F_2 of humic acid in the visible region were significantly reduced in the peak intensity. In addition, the removal efficiency of fulvic acid and humic acid reached 98.29% and 93.14% in the $(\text{Zn}_{0.72}\text{Fe}_{0.28})\text{S}/\text{H}_2\text{O}_2/\text{vis}$ process, respectively. Moreover, the luminescence region of fulvic acid and humic acid of the wastewater after the $(\text{Zn}_{0.72}\text{Fe}_{0.28})\text{S}/\text{H}_2\text{O}_2/\text{vis}$ system treatment has a blue shift, indicating that the decomposition of refractory organic compounds in the wastewater and the break-up of the large molecules into smaller fragments [50].

3.5. Reaction mechanism

As shown in Fig. 7a, the EPR signal intensity of TEMPO in the $(\text{Zn}_{0.72}\text{Fe}_{0.28})\text{S}/\text{H}_2\text{O}_2/\text{vis}$ system was more weakened than that in the $(\text{Zn}_{0.72}\text{Fe}_{0.28})\text{S}/\text{vis}$ system, indicating the addition of H_2O_2 increased the concentration of h^+ . No significant change in EPR signal was observed in the presence of $(\text{Zn}_{0.72}\text{Fe}_{0.28})\text{S}$ and H_2O_2 in the dark, confirming h^+ was not formed during the reaction. A typical signal with characteristic intensity of 1:2:2:1 for $\text{DMPO}\cdot\text{OH}$ adduct was noticed in the presence of $(\text{Zn}_{0.72}\text{Fe}_{0.28})\text{S}$ and H_2O_2 , and a relatively stronger peaks of $\text{DMPO}\cdot\text{OH}$ adduct was also found in the $(\text{Zn}_{0.72}\text{Fe}_{0.28})\text{S}/\text{H}_2\text{O}_2/\text{vis}$ system as more $\cdot\text{OH}$ was generated (Fig. 7b). A $\text{DMPO}\cdot\text{OH}$ signal with low intensity were observed in the $\text{H}_2\text{O}_2/\text{vis}$ system, which was mainly attributed to the

direct photolysis of H_2O_2 to $\cdot\text{OH}$. This also confirmed the addition of H_2O_2 in the $(\text{Zn}_{0.72}\text{Fe}_{0.28})\text{S}$ photocatalytic system enhanced the treatment of oily wastewater, mainly because H_2O_2 enhanced photocatalytic performance rather than the direct oxidation of organic pollutants. The signals of $\text{DMPO}\cdot\text{OH}$ in $(\text{Zn}_{0.72}\text{Fe}_{0.28})\text{S}/\text{vis}$ system was detected at negligible levels. In Fig. 7c, more $\cdot\text{O}_2$ was generated in the $(\text{Zn}_{0.72}\text{Fe}_{0.28})\text{S}/\text{vis}$ system than the $(\text{Zn}_{0.72}\text{Fe}_{0.28})\text{S}/\text{H}_2\text{O}_2/\text{vis}$ system, indicating the addition of H_2O_2 decreased the concentration of $\cdot\text{O}_2$.

Based on the above results and discussion, the possible reaction mechanism for the efficient degradation of organics in the oily wastewater under $(\text{Zn}_{0.72}\text{Fe}_{0.28})\text{S}/\text{H}_2\text{O}_2/\text{vis}$ system could be summarized (Fig. 7d). Under visible light irradiation, when the light energy reached the Eg of $(\text{Zn}_{0.72}\text{Fe}_{0.28})\text{S}$, the photo-generated e^- will be excited from the VB position to the CB (Eq. 1), leaving photo-generated h^+ on VB. Since the CB position of $(\text{Zn}_{0.72}\text{Fe}_{0.28})\text{S}$ was more negative than the $\cdot\text{O}_2/\text{O}_2$ redox potential, the e^- can be reacted with the adsorbed O_2 to form $\cdot\text{O}_2$ radicals (Eq. 2). Some photo-induced e^- may be also captured by H_2O_2 to produce $\cdot\text{OH}$ with stronger oxidation than $\cdot\text{O}_2$ (Eq. 3), which confirmed that the signal of $\text{DMPO}\cdot\text{O}_2$ in the $(\text{Zn}_{0.72}\text{Fe}_{0.28})\text{S}/\text{H}_2\text{O}_2/\text{vis}$ system was weaker than that in $(\text{Zn}_{0.72}\text{Fe}_{0.28})\text{S}/\text{vis}$ system (Fig. 5b). Simultaneously, this process effectively prevented the recombination of $\text{e}^- \cdot \text{h}^+$ pairs, thus more photo-induced h^+ accumulated in VB, which explained the weak EPR signal of TEMPO in $(\text{Zn}_{0.72}\text{Fe}_{0.28})\text{S}/\text{H}_2\text{O}_2/\text{vis}$ system (Fig. 7a). Then, the h^+ left in VB could directly oxidize and degrade organic pollutants instead of reacting with H_2O to form $\cdot\text{OH}$ due to the more negative VB of $(\text{Zn}_{0.72}\text{Fe}_{0.28})\text{S}$ in comparison with that of $\cdot\text{OH}/\text{H}_2\text{O}$ redox potential, this is why there was no $\text{DMPO}\cdot\text{OH}$ signal in the $(\text{Zn}_{0.72}\text{Fe}_{0.28})\text{S}/\text{vis}$ system. In addition, Fe^{2+} on the mineral surface could react with H_2O_2 to form Fe^{3+} and $\cdot\text{OH}$ (Eq. 4). Furthermore, the photo-induced e^- participated the reduction of Fe^{3+} and accelerated the regeneration of Fe^{2+} (Eq. 5), thus ensured the sufficient amount of Fe^{2+} participated in the activation of H_2O_2 . Therefore, the $\text{DMPO}\cdot\text{OH}$ signal in the $(\text{Zn}_{0.72}\text{Fe}_{0.28})\text{S}/\text{H}_2\text{O}_2/\text{vis}$ system was enhanced compared with

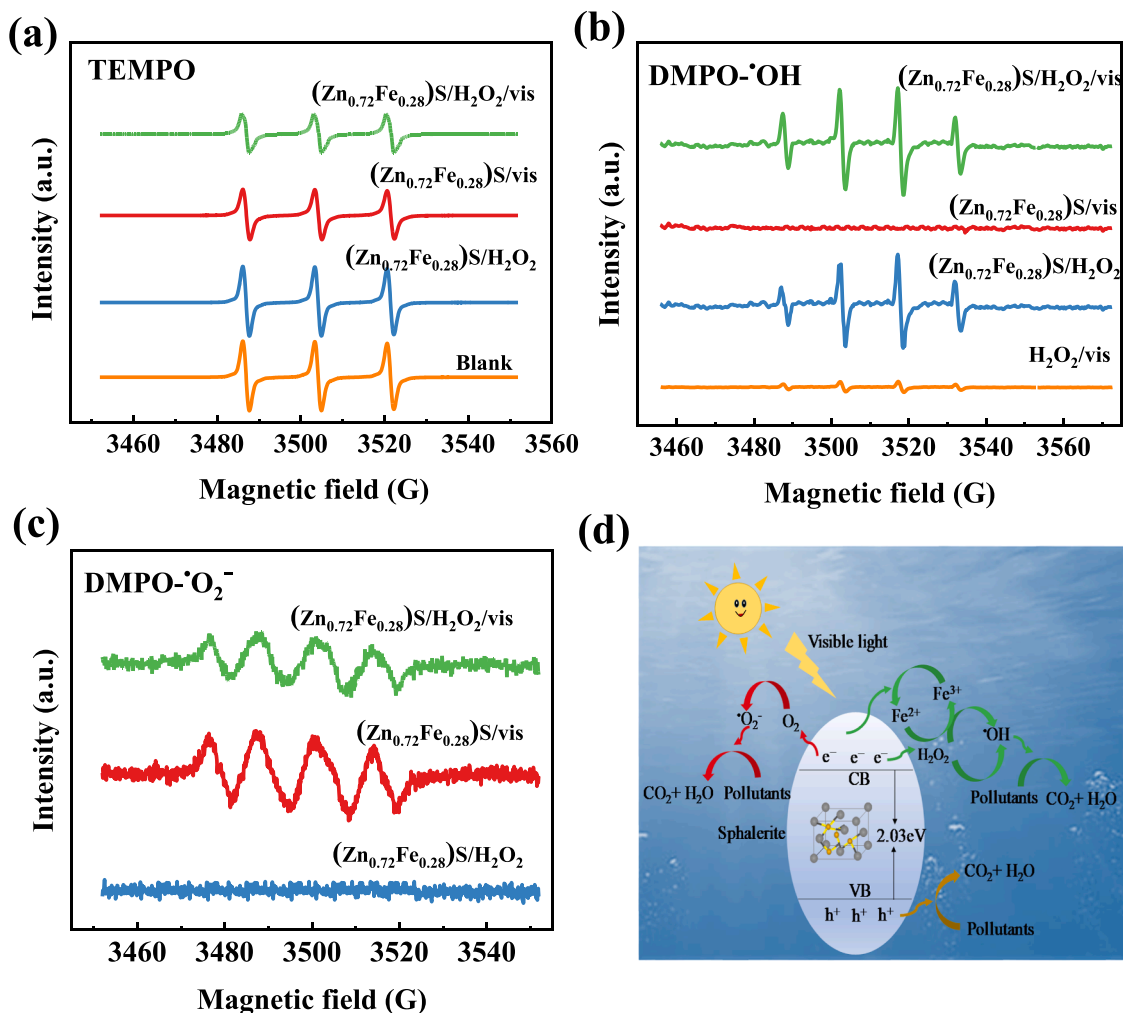


Fig. 7. EPR spectra of (a) TEMPO, (b) DMPO-•OH and (c) DMPO-•O₂⁻ obtained from the different reaction systems. (d) Mechanism of H₂O₂-assisted natural sphalerite photocatalytic treatment of the oily wastewater.

(Zn_{0.72}Fe_{0.28})/H₂O₂ system. Consequently, a better TOC removal efficiency was obtained in (Zn_{0.72}Fe_{0.28})S photocatalysis assisted with H₂O₂ (86.20%) compared with (Zn_{0.72}Fe_{0.28})/H₂O₂ system (59.15%) and (Zn_{0.72}Fe_{0.28})S/vis system (51.27%) (Fig. 4b), which was attributed to the synergistic effects of photocatalysis and Fenton. In conclusion, h⁺, •O₂⁻, and •OH were the main active species contributed to the degradation of organic pollutants in the oily wastewater (Eqs. 6–7).



4. Conclusion

We found a photocatalyst (natural sphalerite ((Zn, Fe)S)) with great application potential for treating oily wastewater of solvent extract from spent LIBs recycling. (Zn_{0.72}Fe_{0.28})S exhibited superior visible-light

absorption ability and carrier mobility among all the (Zn_{1-x}Fe_x)S samples, which was attributed to the doping Fe participated in the formation of new energy bands and accepted transferred-electrons from ZnS as electron acceptor. Consequently, more active species would be produced to degrade organic pollutants in the oily wastewater. 86.20% removal of TOC was achieved with H₂O₂-assisted (Zn_{0.72}Fe_{0.28})S under the optimum conditions of 2 g/L NS, 0.2 mol/L H₂O₂, 101.5 mW·cm⁻² VL intensity and pH = 3.0. This work has reference significance for the treatment of extraction oily wastewater from various industries, especially for the oily wastewater of solvent extraction from spent LIBs recycling.

CRediT authorship contribution statement

Meirong Wu : Conceptualization, Methodology, Data curation, Validation, Writing – original draft. **Shaole Song** : Validation, Investigation. **Tianyu Wang** : Validation, Investigation. **Wei Sun** : Supervision, Investigation. **Shengming Xu** : Supervision, Investigation. **Yue Yang** : Conceptualization, Methodology, Investigation, Writing – review & editing, Supervision.

Declaration of Competing Interest

The authors declare that they have no known competing financial interests or personal relationships that could have appeared to influence the work reported in this paper.

Acknowledgements

The research was supported by the National Key Research and Development Program (2019YFC1907801, 2019YFC1907804), the National Natural Science Foundation of China (No. 51904340, 51834008) and the Natural Science Foundation of Hunan Province (2020JJ4733, 2021JJ20066).

Appendix A. Supporting information

Supplementary data associated with this article can be found in the online version at doi:10.1016/j.apcatb.2022.121460.

References

- [1] Y. Tian, G. Zeng, A. Rutt, T. Shi, H. Kim, J. Wang, J. Koettgen, Y. Sun, B. Ouyang, T. Chen, Z. Lun, Z. Rong, K. Persson, G. Ceder, Promises and challenges of next-generation "Beyond Li-ion" batteries for electric vehicles and grid decarbonization, *Chem. Rev.* 121 (2021) 1623–1669.
- [2] H. Lv, H. Huang, C. Huang, Q. Gao, Z. Yang, W. Zhang, Electric field driven delithiation: a strategy towards comprehensive and efficient recycling of electrode materials from spent lithium ion batteries, *Appl. Catal. B: Environ.* 283 (2021), 119634.
- [3] China Electronic Information Industry Development Research Institute. (<https://www.ccidgroup.com/index.htm>) (Accessed October 20, 2021).
- [4] Global lithium battery market trends and competitive trends in 2018–2025. (<http://www.evpartner.com/news/2017/detail-39730.html>) (Accessed October 20, 2021).
- [5] G. Harper, R. Sommerville, E. Kendrick, L. Driscoll, P. Slater, R. Stoklin, A. Walton, P. Christensen, O. Heidrich, S. Lambert, A. Abbott, K. Ryder, L. Gaines, P. Anderson, Recycling lithium-ion batteries from electric vehicles, *Nature* 575 (2019) 75–86.
- [6] X. Zhang, L. Li, E. Fan, Q. Xue, Y. Bian, F. Wu, R. Chen, Toward sustainable and systematic recycling of spent rechargeable batteries, *Chem. Soc. Rev.* 47 (2018) 7239–7302.
- [7] London Metal Exchange Home Page. (<https://www.lme.com/>) (Accessed October 20, 2021).
- [8] China lithium power grid. (<http://www.cbci.com/li/index.html>) (Accessed October 20, 2021).
- [9] Mineral Commodity Summaries 2021; U.S. Geological Survey. (<https://pubs.er.usgs.gov/publication/mcs2021>) (Accessed October 20, 2021).
- [10] E. Quijada-Maldonado, F. Olea, R. Sepúlveda, J. Castillo, R. Cabezas, G. Merlet, J. Romero, Possibilities and challenges for ionic liquids in hydrometallurgy, *Sep. Purif. Technol.* 251 (2020), 117289.
- [11] J. Jung, P. Sui, J. Zhang, A review of recycling spent lithium-ion battery cathode materials using hydrometallurgical treatments, *J. Energy Storage* 35 (2021), 102217.
- [12] S. Lei, W. Sun, Y. Yang, Solvent extraction for recycling of spent lithium-ion batteries, *J. Hazard. Mater.* 424 (2022), 127654.
- [13] B.S. Al-anzi, O.C. Siang, Recent developments of carbon based nanomaterials and membranes for oily wastewater treatment, *RSC Adv.* 7 (2017) 20981–20994.
- [14] J. Wang, X. Li, G. Ma, H. Sui, L. He, R. Liu, Removal of residual solvent from solvent-extracted unconventional oil ores gangue by gas bubbling, *Sep. Purif. Technol.* 254 (2021), 117551.
- [15] M. Tawalbeh, A. Al Mojily, A. Al Othman, N. Hilal, Membrane separation as a pre-treatment process for oily saline water, *Desalination* 447 (2018) 182–202.
- [16] C. Zhao, J. Zhou, Y. Yan, L. Yang, G. Xing, H. Li, P. Wu, M. Wang, H. Zheng, Application of coagulation/flocculation in oily wastewater treatment: a review, *Sci. Total Environ.* 765 (2021), 142795.
- [17] S.C.R. Marques, J.M. Marcuzzo, M.R. Baldan, A.S. Mestre, A.P. Carvalho, Pharmaceuticals removal by activated carbons: Role of morphology on cyclic thermal regeneration, *Chem. Eng. J.* 321 (2017) 233–244.
- [18] H.J. Tanudjaja, C.A. Hejase, V.V. Tarabara, A.G. Fane, J.W. Chew, Membrane-based separation for oily wastewater: a practical perspective, *Water Res.* 156 (2019) 347–365.
- [19] S. Jamaly, A. Giwa, S.W. Hasan, Recent improvements in oily wastewater treatment: progress, challenges, and future opportunities, *J. Environ. Sci.* 37 (2015) 15–30.
- [20] L. Jing, B. Chen, B. Zhang, P. Li, Process simulation and dynamic control for marine oily wastewater treatment using UV irradiation, *Water Res.* 81 (2015) 101–112.
- [21] L. Ma, J. He, J. Wang, Y. Zhou, Y. Zhao, Y. Li, X. Liu, L. Peng, M. Qu, Functionalized superwetttable fabric with switchable wettability for efficient oily wastewater purification, in situ chemical reaction system separation, and photocatalysis degradation, *ACS Appl. Mater. Interfaces* 11 (2019) 43751–43765.
- [22] M. Moradi, F. Hasanvandian, A.A. Isari, F. Hayati, B. Kakavandi, S.R. Setayesh, CuO and ZnO co-anchored on g-C₃N₄ nanosheets as an affordable double Z-scheme nanocomposite for photocatalytic decontamination of amoxicillin, *Appl. Catal. B: Environ.* 285 (2021), 119838.
- [23] J. Kang, L. Lu, W. Zhan, B. Li, D. Li, Y. Ren, D. Liu, Photocatalytic pretreatment of oily wastewater from the restaurant by a vacuum ultraviolet/TiO₂ system, *J. Hazard. Mater.* 186 (2011) 849–854.
- [24] Y. Zhou, W. Li, W. Wan, R. Zhang, Y. Lin, W/Mo co-doped BiVO₄ for photocatalytic treatment of polymer-containing wastewater in oilfield, *Superlattices Microstruct.* 82 (2015) 67–74.
- [25] D. Hu, X. Yu, M. Zhang, J. Guo, X. Zheng, Study on the photocatalytic degradation of diesel pollutants in seawater by a sonochemically prepared nano zinc oxide, *Adv. Mater. Res.* 476–478 (2012) 1939–1942.
- [26] T. Wang, Y. Zhang, J. Pan, B. Li, L. Wu, B. Jiang, Hydrothermal reduction of commercial P25 photocatalysts to expand their visible-light response and enhance their performance for photodegrading phenol in high-salinity wastewater, *Appl. Surf. Sci.* 480 (2019) 896–904.
- [27] W. Wang, G. Li, D. Xia, T. An, H. Zhao, P. Wong, Photocatalytic nanomaterials for solar-driven bacterial inactivation: recent progress and challenges, *Environ. Sci. Nano* 4 (2017) 782–799.
- [28] G. Li, X. Chen, H. Yin, W. Wang, P. Wong, T. An, Natural sphalerite nanoparticles can accelerate horizontal transfer of plasmid-mediated antibiotic-resistance genes, *Environ. Int.* 136 (2020), 105497.
- [29] Y. Chen, A. Lu, Y. Li, L. Zhang, H. Yip, H. Zhao, T. An, P. Wong, Naturally occurring sphalerite as a novel cost-effective photocatalyst for bacterial disinfection under visible light, *Environ. Sci. Technol.* 45 (2011) 5689–5695.
- [30] H. Yin, X. Chen, G. Li, W. Wang, P. Wong, T. An, Can photocatalytic technology facilitate conjugative transfer of ARGs in bacteria at the interface of natural sphalerite under different light irradiation? *Appl. Catal. B: Environ.* 287 (2021), 119977.
- [31] Y. Li, A. Lu, S. Jin, C. Wang, Photo-reductive decolorization of an azo dye by natural sphalerite: case study of a new type of visible light-sensitized photocatalyst, *J. Hazard. Mater.* 170 (2009) 479–486.
- [32] J. Deng, H. Lai, M. Chen, M. Glen, S. Wen, B. Zhao, Z. Liu, H. Yang, M. Liu, L. Huang, S. Guan, P. Wang, Effect of iron concentration on the crystallization and electronic structure of sphalerite/marmatite: A DFT study, *Miner. Eng.* 136 (2019) 168–174.
- [33] Q. Wang, P. Xu, G. Zhang, L. Hu, P. Wang, Visible-light responsive g-C₃N₄ coupled with ZnS nanoparticles via a rapid microwave route: characterization and enhanced photocatalytic activity, *Appl. Surf. Sci.* 488 (2019) 360–369.
- [34] D. Wu, W. Wang, T.W. Ng, G. Huang, D. Xia, H.Y. Yip, H.K. Lee, G. Li, T. An, P. K. Wong, Visible-light-driven photocatalytic bacterial inactivation and the mechanism of zinc oxysulfide under LED light irradiation, *J. Mater. Chem. A* 4 (2016) 1052–1059.
- [35] Y. Liao, Y. Xia, S. Zou, P. Liu, X. Liang, S. Yang, In situ emergency disposal of liquid mercury leakage by Fe-containing sphalerite: performance and reaction mechanism, *Ind. Eng. Chem. Res.* 56 (2016) 153–160.
- [36] Y. Li, A. Lu, C. Wang, X. Wu, Characterization of natural sphalerite as a novel visible light-driven photocatalyst, *Sol. Energy Mater. Sol. Cells* 92 (2008) 953–959.
- [37] L. Li, C. Lai, F. Huang, M. Cheng, G. Zeng, D. Huang, B. Li, S. Liu, M. Zhang, L. Qin, M. Li, J. He, Y. Zhang, L. Chen, Degradation of naphthalene with magnetic bio-char activate hydrogen peroxide: synergism of bio-char and Fe-Mn binary oxides, *Water Res.* 160 (2019) 238–248.
- [38] X. Du, C. Li, L. Zhao, J. Zhang, L. Gao, J. Sheng, Y. Yi, J. Chen, G. Zeng, Promotional removal of HCHO from simulated flue gas over Mn-Fe oxides modified activated coke, *Appl. Catal. B: Environ.* 232 (2018) 37–48.
- [39] J. Li, Z. Xiong, Y. Yu, X. Wang, H. Zhou, B. Huang, Z. Wu, C. Yu, T. Chen, Z. Pan, G. Yao, B. Lai, Efficient degradation of carbamazepine by electro-Fenton system without any extra oxidant in the presence of molybdate: the role of slow release of iron ions, *Appl. Catal. B: Environ.* 298 (2021), 120506.
- [40] D. Xia, T.W. Ng, T. An, G. Li, Y. Li, H.Y. Yip, H. Zhao, A. Lu, P.K. Wong, A recyclable mineral catalyst for visible-light-driven photocatalytic inactivation of bacteria: natural magnetic sphalerite, *Environ. Sci. Technol.* 47 (2013) 11166–11173.
- [41] Y. Wang, L. Rao, P. Wang, Z. Shi, L. Zhang, Photocatalytic activity of N-TiO₂/O-doped N vacancy g-C₃N₄ and the intermediates toxicity evaluation under tetracycline hydrochloride and Cr(VI) coexistence environment, *Appl. Catal. B: Environ.* 262 (2020), 118308.
- [42] V.I. Anisimov, F. Aryasetiawan, A.I. Lichtenstein, First-principles calculations of the electronic structure and spectra of strongly correlated systems: the LDA+U method, *J. Phys. Condens. Matter* 9 (1997) 767–808.
- [43] X. Hao, Y. Wang, J. Zhou, Z. Cui, Y. Wang, Z. Zou, Zinc vacancy-promoted photocatalytic activity and photostability of ZnS for efficient visible-light-driven hydrogen evolution, *Appl. Catal. B: Environ.* 221 (2018) 302–311.
- [44] Y. Chen, J. Chen, J. Guo, A. DFT, study on the effect of lattice impurities on the electronic structures and floatability of sphalerite, *Miner. Eng.* 23 (2010) 1120–1130.
- [45] P. Wang, S. Zhan, Y. Xia, S. Ma, Q. Zhou, Y. Li, The fundamental role and mechanism of reduced graphene oxide in rGO/Pt-TiO₂ nanocomposite for high-performance photocatalytic water splitting, *Appl. Catal. B: Environ.* 207 (2017) 335–346.
- [46] S. Xiong, S. Bao, W. Wang, J. Hao, Y. Mao, P. Liu, Y. Huang, Z. Duan, Y. Lv, D. Ouyang, Surface oxygen vacancy and graphene quantum dots co-modified Bi₂WO₆ toward highly efficient photocatalytic reduction of CO₂, *Appl. Catal. B: Environ.* 305 (2022), 121026.
- [47] X. Wang, X. Wang, W. Tian, A. Meng, Z. Li, S. Li, L. Wang, G. Li, High-energy ball-milling constructing P-doped g-C₃N₄/MoP heterojunction with Mo N bond bridged interface and Schottky barrier for enhanced photocatalytic H₂ evolution, *Appl. Catal. B: Environ.* 303 (2022), 120933.

- [48] A. Baker, M. Curry, Fluorescence of leachates from three contrasting landfills, *Water Res.* 38 (2004) 2605–2613.
- [49] W. Chen, Y. Luo, G. Ran, Q. Li, An investigation of refractory organics in membrane bioreactor effluent following the treatment of landfill leachate by the O_3/H_2O_2 and MW/PS processes, *Waste Manag.* 97 (2019) 1–9.
- [50] Z. Wang, Z. Wu, S. Tang, Characterization of dissolved organic matter in a submerged membrane bioreactor by using three-dimensional excitation and emission matrix fluorescence spectroscopy, *Water Res.* 43 (2009) 1533–1540.